



Hierarchical toughening mechanisms in face centered cubic CoCrFeMnNi high-entropy alloy at room temperature and cryogenic temperatures

Cheng Huang,^{1,2} Yin Yao,² Bo Yang³, and Shaohua Chen^{2,*}

¹College of Aerospace Engineering, Chongqing University, Chongqing 400044, China

²Institute of Advanced Structure Technology and Beijing Key Laboratory of Lightweight Multi-functional Composite Materials and Structures, Beijing Institute of Technology, Beijing 100081, China

³School of Mechanical Engineering, Research Centre for Technological Innovation Method and Tool, Hebei University of Technology, Tianjin 300401, China



(Received 5 June 2022; revised 8 January 2023; accepted 21 March 2023; published 5 May 2023)

As a class of promising structural material, recently synthesized face centered cubic phased high-entropy alloys (HEAs) exhibit excellent room-temperature (RT) fracture toughness as well as an abnormally increasing one at cryogenic temperatures (CTs). The intrinsic toughening mechanisms are not yet well understood. Attention here is focused on the atomistic crack initiation and propagation in a model HEA CoCrFeMnNi under RT and CTs, by means of atomistic simulations integrated with theoretical analysis. Hierarchical deformation mechanisms of the incipient plasticity; the local amorphization; and the formation, growth, and coalescence of voids are found, based on which the strain energy stored in the material is continually dissipated, resulting in the outstanding fracture toughness of the HEA at both RT and CTs. The origin for low-temperature toughening may be attributed to fewer immobile dislocations at CTs, delaying the occurrence of amorphization and microvoids. The differences in mechanisms for low-temperature toughening of the HEA and low-temperature embrittlement of traditional metals are further comparatively revealed. This study provides mechanistic insights into the fundamental understanding of intrinsic toughening mechanisms in the HEA.

DOI: [10.1103/PhysRevB.107.174103](https://doi.org/10.1103/PhysRevB.107.174103)

I. INTRODUCTION

Metals and their alloys play crucial roles in modern industries. However, the performances of traditional alloys reach a bottleneck in the way that a single principle element is mixed with a small number of other elements [1]. In recent years, high-entropy alloys (HEAs) composed of multiple principle elements have attracted broad interests because of their unique compositions, microstructures, and adjustable properties [2–5]. Accordingly, four core effects, including high entropy, sluggish diffusion, severe lattice distortion, and cocktail, are summarized by Tsai and Yeh [6], leading to excellent properties of HEAs, such as high strength [7–9]; good tensile ductility [10,11]; outstanding fracture toughness [12–14]; high specific strength [2]; and exceptional resistance to corrosion [15], irradiation [16,17], and high temperature [18].

As a class of promising structural materials, strength and fracture toughness of HEAs are two extremely important mechanical properties in practical applications [19,20]. Usually, it is difficult for traditional alloys to achieve a good synergy between strength and toughness [21,22], while it was recently found that the single solid solution face centered cubic (fcc) phased HEAs, such as CoCrFeMnNi HEA and its derivatives, exhibit an excellent combination of strength, ductility, and fracture toughness. For example, the yield strength and

ultimate tensile strength of CoCrFeMnNi HEA are about 300 MPa and 1 GPa, respectively [23]; the tensile ductility exceeds 60%; and the fracture toughness is 200 MPa m^{0.5} [13] at room temperature (RT), which could be further improved at cryogenic temperatures (CTs) [13,23,24]. Such mechanical behaviors are totally different from those of traditional alloys. For traditional alloys, good fracture toughness can be achieved at RT in the way of ductile fracture, while a transition from ductile to brittle fracture occurs when decreasing the temperature [25]. The microscopic mechanism for a brittle fracture is that the crack propagates along a cleavage crystallographic plane due to high stress concentration at the crack tip [26], while the microscopic mechanism for a ductile fracture is that dislocations nucleate and propagate from the crack tip [27]. This means that the transition from ductile to brittle fracture is a result of transition from dislocation activity to bond breakage. In other words, whether the transition occurs is the result of competition between these two mechanisms. This brings about a fundamental problem of what mechanisms govern the intrinsic room-temperature fracture toughness and the abnormally increasing low-temperature toughening in fcc-phased HEAs.

To explore the underlying mechanisms of damage tolerance of the fcc-phased HEAs, *in situ* straining in a transmission electron microscope (TEM) was used [28]. Plastic deformation, involving stacking faults and partial dislocations, is found near the crack tip at RT. The TEM observation provides strong evidence for the ductile fracture of HEA at RT; the real-time evolution of fracture at nanoscale

*Corresponding author: chenshaohua72@hotmail.com

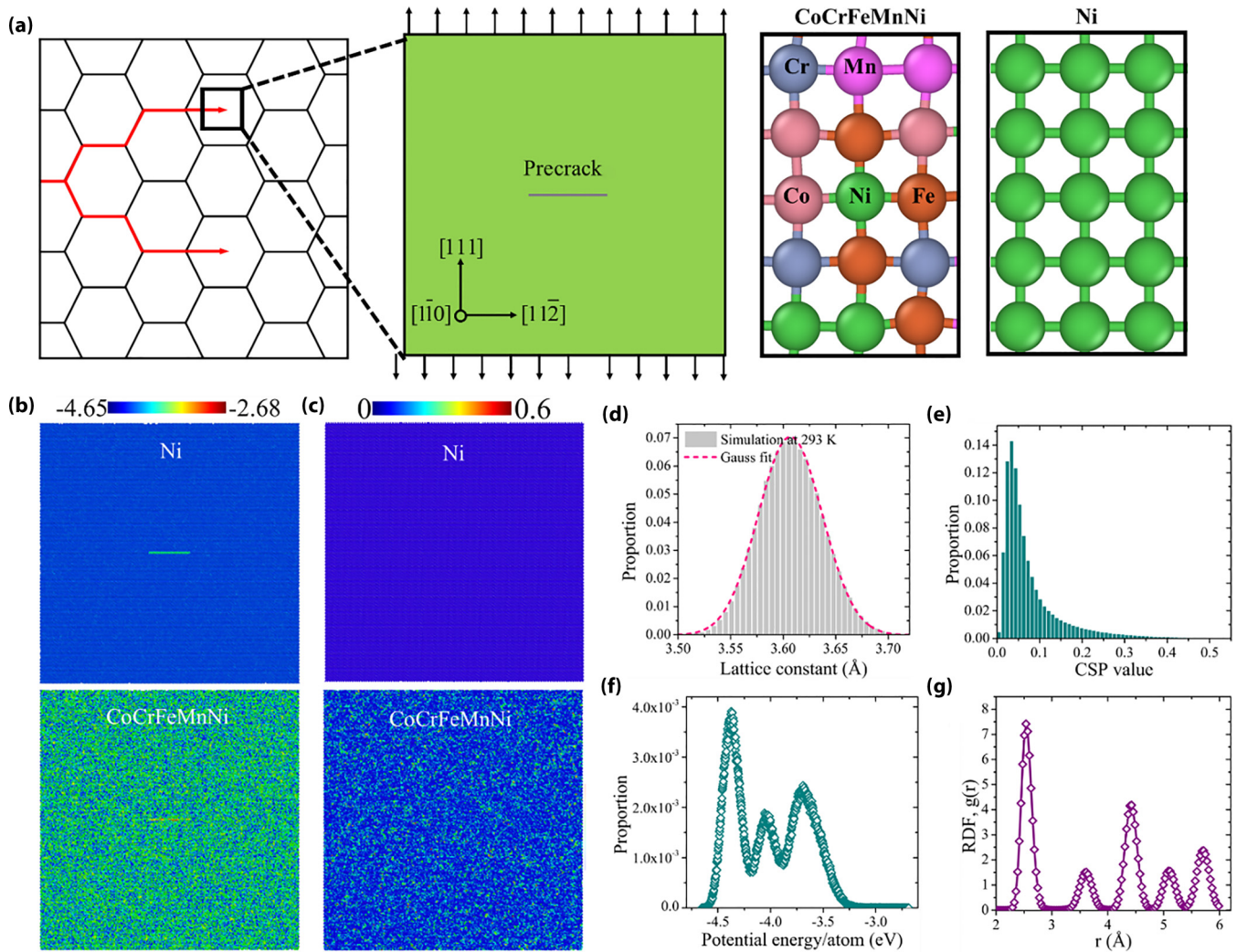


FIG. 1. Atomic-scale characterization of lattice distortion in the HEA. (a) Schematic diagram for uniaxial tension simulation of crack propagation. The simulated model shows a precrack located in the center region, and the loading direction is perpendicular to the crack surface. (b) Distributions of the atomic potential energies in the HEA and Ni after energy minimization and temperature relaxation at RT. (c) CSP distributions in the HEA and Ni after energy minimization and temperature relaxation at RT. (d) Histogram of the lattice constant distribution of HEA. (e) Histogram of CSP distribution of HEA. (f) Proportion of the atomic potential energies of the HEA. (g) The radial pair distribution function of the HEA as a function of pair distance.

is, however, inaccessible in experiments, and the intrinsic mechanisms for the ultrahigh fracture toughness is not yet well understood at RT, not to mention the unusually enhancing fracture toughness at CTs.

Here, the toughening mechanisms of the single solid solution fcc-phased HEA at RT and CTs are studied by means of large-scale molecular dynamics (MD) simulations and theoretical analysis. Representative CoCrFeMnNi HEA and pure Ni metal are selected for comparison. The simulations show that the ultrahigh fracture toughness of the HEA at both RT and CT originates from the hierarchical deformation mechanisms in the vicinity of the crack tip, including partial dislocations, deformation twins, crystalline phase transformations, dislocation interactions, local amorphous phase transformations, formation, growth, and coalescence of microvoids. Furthermore, fewer immobile dislocations in the HEA at CTs may be a reason for the delay of the occurrence of the local amorphous phase transformation

and microvoids, leading to higher fracture toughness. The differences in mechanisms for the low-temperature toughening of the HEA and low-temperature embrittlement of traditional metals are further comparatively revealed. The results disclose the fundamental toughening mechanisms in the HEA, which should also be useful for the design of engineering structural materials with high performance.

II. METHODS

A. Atomistic model with precrack

Nanoscale CoCrFeMnNi HEA and pure Ni samples with precracks provide a model system to study the atomistic crack propagation and toughening mechanisms. Figure 1(a) presents the schematic diagram for uniaxial tension simulations of crack propagation in the two materials with a typical mode I loading, the size of which is about 50, 50, and 2 nm in the x , y , and z directions, corresponding to the crystal orientations

of $[11\bar{2}]$, $[1\bar{1}0]$, and $[111]$, respectively. An initially sharp edge precrack with a length of 8 nm is introduced into the middle of each sample by eliminating the interaction across the upper and lower surfaces of the crack. The crack surface is on the $[111]$ plane, and the crack front is along the $[1\bar{1}0]$ direction. This kind of method upon introduction of a precrack is commonly used in atomistic simulations [29].

B. Mode I loading simulation of fracture

MD simulations are performed with large-scale atomic/molecular massively parallel simulator (LAMMPS) [30]. The well-established parameters of the second nearest neighbor modified embedded-atom method (2NN MEAM) potential proposed by Choi *et al.* [31] are adopted for describing the interactions among atoms in CoCrFeMnNi HEA and pure Ni metal. This potential is widely used in the MD simulations of CoCrFeMnNi HEA and its derivatives [32–34]. The simulations are conducted as follows. Firstly, the conjugate gradient algorithm is applied on each numerical sample to optimize the initial atomic configuration. Then, each sample is relaxed at RT and CTs for 50 ps under *NPT* (constant number of atoms, pressure, and temperature) ensemble. After that, uniaxial tension simulations are finally performed along the y direction at a constant strain rate of 1/ns, and different temperature under *NVT* (constant number of atoms, volume, and temperature) ensemble. The *NVT* ensemble is used when performing time integration on Nosé-Hoover style non-Hamiltonian equations of motion for generating and updating atomic positions and velocities. During each time step Δt , the sample is firstly stretched for a certain length increment Δl , and then the updated system is relaxed at the given temperature under the *NVT* ensemble. The whole tension process is the computational iteration of each time step. In this case, only the length along the tension direction is stretched, while the cross-sectional area is fixed. This method can result in plane-strain deformation, which is similar to the opening-mode crack propagation in thick plates. In fact, this method is commonly adopted in MD simulations when studying the fracture process of a material with precrack [35–39]. The boundary conditions are periodic for the three directions. The atoms are kept at constant target temperatures by a Langevin thermostat. Deformation analysis is assisted by the open visualization tool (OVITO) [40], associated with the dislocation extraction algorithm (DXA) [41] and polyhedral template matching (PTM) [42] for tracking the evolution of crystal defects in real time.

C. Calculation of surface energy

The MD simulation model for calculating the surface energies of the HEA is shown in Fig. 6(a), where an initially perfect HEA slab is separated into two slabs, generating two new surfaces, and then the surface energy can be obtained. Thus the surface energy can be written as

$$\gamma_{\text{surf}} = \frac{E_1 - E}{2A}, \quad (1)$$

where E_1 , E , and A are the total energies of a material with and without new surfaces, and the area of the new surface, respectively.

D. Calculation of stacking fault energy

The MD simulation model for calculating the generalized stacking fault energies of the HEA is shown in Fig. 6(b). The upper and lower parts of an initially perfect HEA single crystal slide relative to each other, forming a stacking fault, and then the stacking fault energy can be obtained. Thus the stacking fault energy can be written as

$$\gamma_{\text{GSFE}} = \frac{E_x - E}{A_x}, \quad (2)$$

where E_x , E , and A_x are the total energies of a material before and after a relative displacement x , and the area of the stacking fault, respectively.

E. Calculation of local state of stress

At the nanoscale, the local stress state in a solid is usually measured by the virial stress. Based on the virial theorem, the local atomic stress is defined as

$$\sigma_{\alpha\beta} = \frac{1}{\Omega} \left(\sum_i m_i v_{i\alpha} v_{i\beta} + \frac{1}{2} \sum_{i \neq j} r_{ij\beta} F_{ij\alpha} \right), \quad (3)$$

in which m_i and v_{i*} are the mass and velocity components of the atom i , r_{ij} and F_{ij} are the distance and interaction force components between the atoms i and j along the coordinate axis, and Ω is the atomic volume.

III. RESULTS

A. Lattice distortion in the HEA

Lattice distortion, as one of the core effects of HEAs [6], is considered to be one of the key factors leading to excellent performance [7,8], which is caused by the atomic size difference of different elements. Although the differences are not so obvious, they can still induce homogeneously distributed lattice distortions compared to the traditional metals and alloys. To characterize the lattice distortion in the HEA, the lattice constant, the radial pair distribution function (RDF), the center-symmetry parameter (CSP), and the atomic potential energy are calculated. The RDF measures the probability of finding a particle at a given distance r , which is commonly used to detect the state of particle distribution in a system [43,44]. The CSP is a useful measurement of local lattice disorder around an atom, which is defined as [45]

$$p = \sum_{i=1}^{N/2} |r_i + r_{i+N/2}|, \quad (4)$$

where N is the number of the nearest neighbors of an atom, and r_i and $r_{i+N/2}$ are two neighbor vectors from the central atom to a pair of opposite neighboring atoms. For lattice sites in an ideal centrosymmetric crystal, the contribution of all neighboring pairs in Eq. (1) will cancel, and the resulting CSP value will be zero. Figure 1(b) shows the distribution of the atomic potential energies in the HEA after energy

TABLE I. Atomic potential energies of the HEA and the individual pure metals. The pure metals Cr, Fe, and Mn are bcc structures, Co is hcp lattice, and Ni is fcc lattice at room and cryogenic temperatures.

Materials	Ni	Co	Cr	Fe	Mn	Average	HEA
Energy (eV)	-4.4116	-4.3709	-4.0608	-4.2508	-2.8578	-4.5619	-4.0090

minimization and temperature relaxation at RT, where those of pure metal Ni are also given for comparison. There are distinct peaks in the energy distribution in the HEA. To make clear if the atomic potential energy of the HEA is significantly different from an average of the individual lattice structures, we further calculated the atomic potential energies of five pure metals composed of the five individual elements. The individual pure metals Cr, Fe, and Mn are body-centered cubic (bcc) structures, Co is hexagonal close-packed (hcp) lattice, and Ni is fcc lattice at room and cryogenic temperatures. The calculated atomic potential energies are shown in Table I, where it can be seen that the potential energy of the HEA is quite different from that of the average of the individual structures, which might be induced by the lattice distortion of the HEA. In fact, atomic lattice distortion in the CoCrFeMnNi HEA was previously observed by high-resolution transmission electron microscopy (HRTEM), which has been proved to delay the motion of dislocations [46]. Similarly, the CSP distribution in Fig. 1(c) also indicates that the HEA is not an ideal centrosymmetric crystal. The RDF, the proportions of the lattice constant, CSP value, and atomic potential energy of the HEA are further shown in Figs. 1(d)–1(g). The lattice constant of HEA at RT follows the Gaussian distribution with a statistical value of 0.3606 ± 0.006 11 nm [Fig. 1(d)], which demonstrates the lattice distortion and atomic level heterogeneity in HEA [7,47]. The peaks of the RDF curve are blunt [Fig. 1(g)], which indicates that the neighboring distance of atoms is not constant. The CSP values for almost all the atoms are higher than zero [Fig. 1(e)], and there are also distinct peaks in the atomic potential energy distributions [Fig. 1(f)]. All these results clearly demonstrate that the atomic-scale lattice distortion is an important structural feature in HEAs, which should obviously affect the physical properties of the material.

B. Fracture properties of the HEA

The stress-strain relation of HEA under uniaxial tension at RT and CTs is shown in Fig. 2(a), where that of traditional Ni metal at different temperatures is also included for comparison. At RT, both the stress of pure Ni and that of CoCrFeMnNi HEA slowly decrease after the maximum value, exhibiting a typical ductile fracture, whereas the maximum strain of HEA is much higher than that of pure Ni metal. The former reaches 47%, while the latter is only 27%. Greater differences are seriously reflected in the low-temperature fracture properties. As the temperature decreases to CT, the fracture stress of both the HEA and pure Ni metal increases slightly. However, the fracture strain of two materials shows apparent difference. The fracture strain of the HEA decreases inconsiderably, while that of Ni decreases obviously. When the temperature reaches the liquid nitrogen temperature, i.e., 77 K, or the liquid helium temperature, i.e., 4.2 K, the stress of Ni reaches the

peak and then drops dramatically to zero, indicating a typical brittle fracture behavior. Notably, temperature dependence of the fracture toughness of HEA and Ni shows a completely opposite law. We note that the present simulations cannot properly measure the ductility of the material, i.e., the well-known necking phenomenon of a metallic material, since we adopt the generic periodic boundary conditions (PBCs) for representing bulk material.

Figure 2(a) shows much higher stress levels compared with real experiments. The first reason is that the strain rate in MD simulations is inevitably large. Secondly, the MD simulation model used in our simulation is single crystalline with a precrack, while the samples with precrack in real experiments are usually polycrystalline. The last reason is that the value of a MD simulation can be affected by many factors, such as sample size, precrack size, loading mode (displacement loading, strain rate loading, etc.), atomic potential function, parameters, etc. To sum up, MD simulations can qualitatively reveal some phenomena that are difficult to observe in experiments, but cannot give the exact mechanical properties quantitatively. The stress of the single crystalline HEA with a precrack under a strain rate of 1×10^9 /s could not be regarded as near-theoretical strengths of the material. Zhang *et al.* [36] comparatively studied the fracture of graphene with

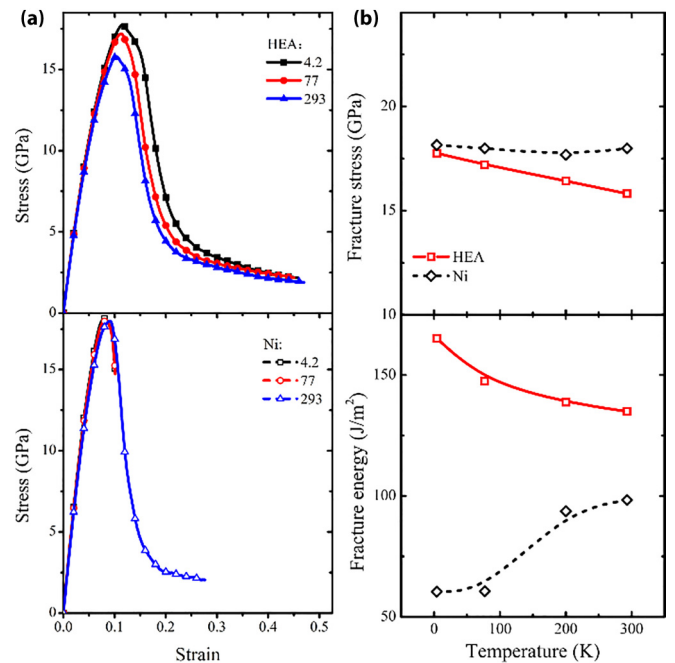


FIG. 2. Overall mechanical response of the HEA and pure Ni with precracks under mode I loading. (a) The stress-strain curves of the HEA and pure Ni metal at RT and CTs, respectively. (b) The fracture stress and fracture energy of the HEA and pure Ni as a function of the temperature.

a precrack from both experiments and MD simulations. Their MD simulation result is about seven to ten times as big as the experimental results. The second example is the comparison of fracture of graphene with prevoids by MD simulations from different references. Liu *et al.* [48] and Cohen-Tanugi and Grossman. [49] studied the fracture of single crystalline graphene with prevoids, separately, but the fracture stresses of the material with the same void size are much different. In addition, Zhang *et al.* [50] studied the fracture of polycrystalline graphene with prevoids, the stress of which is extremely lower than those of the above single crystals with prevoids. The third example is a comparative study of uniaxial tensile responses of a nanotwinned metal from both experiments and MD simulations [51]. Their results showed that the finite element results are consistent with the experimental results, while the stresses of MD simulation results are about six to ten times larger than those of the experiments. Thus the fracture strength or yield strength of a material with precracks or prevoids still much higher than that obtained in real experiments.

In spite of the fact that extremely high strain rate is commonly used in MD simulations [52–54], we still perform additional fracture simulation of the HEA with an order of magnitude slower strain rate. The strain rate effect is shown by a comparison of the mechanical response of the HEA at RT under strain rates of 1×10^8 and 1×10^9 /s, respectively (shown in Fig. S1 in the Supplemental Material [55]). It is found that the fracture stress and the fracture energy of the lower strain rate are smaller than those of the higher strain rate. Importantly, the strain rate has a lesser effect on the deformation of fracture. Figure S1(b) [55] shows the corresponding hierarchical fracture deformation of the HEA under a strain rate of 1×10^8 /s, which includes the incipient plasticity, the local amorphization, and the dynamic evolution of voids, consistent with that of 1×10^9 /s.

The fracture stress and fracture energy of both the HEA and Ni are shown in Fig. 2(b) as a function of temperature. The fracture stress is adopted as the maximum stress of each curve, and the fracture toughness is characterized by the fracture energy, which can be obtained by multiplying the integrated area under the stress-strain curve by the width of the simulated sample [29,56]. This shows that the fracture stress of both the HEA and Ni increases with the decrease of temperature, except that the former is more apparent. Such a result is also consistent with the temperature-dependent fracture stress of crystalline solids [25]. However, the fracture energy of the HEA will increase from 134.92 J/m^2 at RT to 165.08 J/m^2 at CTs, which is well consistent with previous experimental results [13,24,57]. In contrast, the fracture energy of Ni decreases remarkably from 98.34 J/m^2 at RT to 60.42 J/m^2 at CTs. This indicates that the fracture toughness of face centered cubic HEA is enhanced at CTs, which is quite different from that of traditional metals and alloys. What mechanisms govern the intrinsic toughness of the HEA and induce the abnormal low-temperature toughening?

C. Hierarchical toughening mechanisms at RT

To make clear the underlying mechanisms for the intrinsically high fracture toughness of the fcc-phased HEA at RT, we shed light on its atomic-scale crack propagation and

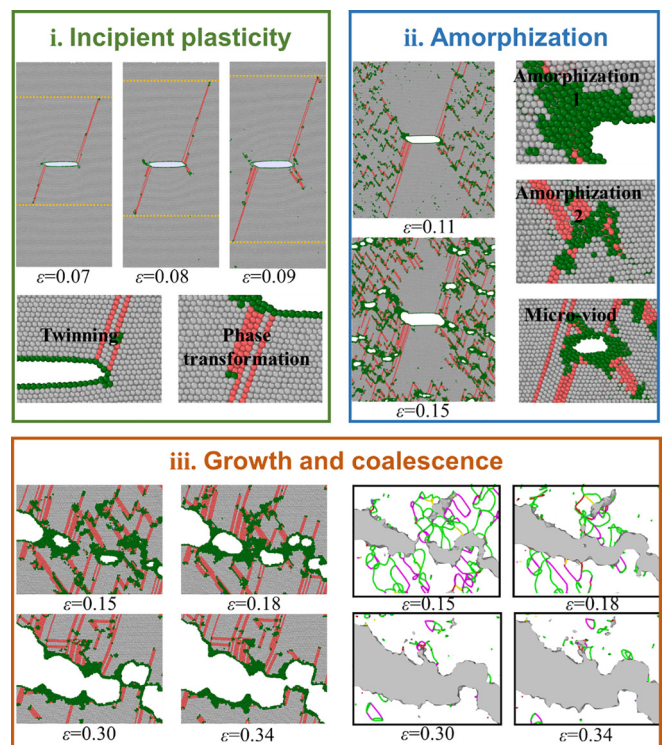


FIG. 3. Hierarchical toughening mechanisms of the HEA at RT. The fracture propagation process can be divided into three levels, i.e., the incipient plasticity, the amorphous phase transition, and the dynamic evolution of voids. The atoms are colored with the polyhedral template matching (PTM) method, where the red, gray, and green balls denote atoms arranged in HCP lattice, fcc lattice, and disordered state, respectively. The green, pink, and yellow lines denote Shockley partial dislocations, stair-rod dislocations, and Hirth dislocations, respectively, and the gray regions represent surfaces or interfaces, which are extracted and colored with the dislocation extraction algorithm (DXA).

deformation behaviors as shown in Fig. 3. Hierarchical toughening mechanisms are found to be responsible for intrinsic toughening of the HEA at RT, which can be generally divided into three levels, i.e., the incipient plasticity; the local amorphization; and the formation, growth, and coalescence of voids.

Level I: The incipient plasticity. The initially closed crack in the sample is opened when subjected to mode I loading, but the crack does not start to propagate. When the strain reaches 0.037, Shockley partial dislocations and associated stacking faults nucleate from the crack tip. With further straining, new Shockley partial dislocations nucleate and expand from adjacent positions near the tip of crack, resulting in the transition from stacking faults to deformation twinning and phase transformation. Figure S2 [55] gives the possible deformation paths of incipient plasticity in the HEA, and calculates the generalized planar fault energies for the paths. The results show that the energy barriers needed for deformation twinning and fcc to HCP phase transformation are close, which indicates that both deformation behaviors and their couplings can contribute to the incipient plasticity. The incipient plasticity found in our present simulations, including

the formations of Shockley partial dislocations, deformation twins, and crystalline phase transformations from the crack tip, agrees well with the previous TEM observations [28]; this makes the initially sharp crack tip blunt, and reduces stress concentration at the crack tip, and dissipates the strain energy stored in the material. It is thought to be an important nanoscale origin for the ultrahigh damage tolerance of the HEA. Thus the incipient plasticity instead of crack propagation contributes to the ductile fracture of the HEA in the initial deformation stage.

Level II: The local amorphization. It was found in the previous experiments that the lattice distortion can affect the stacking fault energy and activation barrier for the motion of dislocations [58,59]. As loading continues, as shown in part I of Fig. 3, the motion of dislocations is not uniform; somewhere dislocations would move faster, while somewhere dislocations would move slower, since there are distinct peaks and valleys in the energy distribution (Fig. 1), resulting from the atomic-level heterogeneity. The unstable dislocation motion makes the dislocation lines meandering [Fig. 4(a)], and then promotes their interaction of dislocations, which are consistent with previous experiments [46,58]. In order to meet the compatibility of deformation, cross slips take place among the hindered dislocations, resulting in the formation of local amorphization from the sites of cross slips. It is interesting that such a behavior of local amorphous phase transformation was also found in experiment when extreme deformation occurs [60], as a particular route to dissipate the strain energy stored in the material.

As for the formation mechanism of local amorphization, we shed light on the interaction of dislocations near the crack tip in the HEA, as shown in Fig. 4(a). Shockley partial dislocations are firstly emitted from the crack tip, and then the planar slips of these dislocations are delayed due to lattice distortion of the HEA [$\varepsilon = 0.075$ in Fig. 4(a)]. The wriggling Shockley partial dislocations interact with each other with the following mode:

$$\frac{1}{6}[2\bar{1}\bar{1}] + \frac{1}{6}[\bar{1}\bar{2}1] \rightarrow \frac{1}{6}[1\bar{1}0]. \quad (5)$$

As a result $\frac{1}{6}[1\bar{1}0]$, called a stair-rod dislocation, is formed [$\varepsilon = 0.08$ in Fig. 4(a)]. It is a kind of immobile dislocation marked with pink lines in Fig. 4(a). Thus the planar slips of Shockley partial dislocations can be hindered by the stair-rod dislocations after the dislocation reaction occurs, resulting in the pinning of Shockley partial dislocations at the interaction sites [$\varepsilon = 0.095$ and $\varepsilon = 0.1$ in Fig. 4(a)]. As a result, the plastic deformation of HEA cannot be contributed to by the planar slips of Shockley partial dislocations [$\varepsilon = 0.1$ in Fig. 4(a)], and local stress accumulation occurs at the pinning sites. To dissipate the strain energy stored in HEA, and reduce the local stress concentration, continuous transitions from crystalline state to amorphous state occur at the pinning sites [$\varepsilon = 0.115$ and $\varepsilon = 0.12$ in Fig. 4(a)]. Thus the dislocation interaction and local amorphization contribute to the ductile fracture of HEA in this second stage.

Level III: Formation, growth, and coalescence of microvoids. When it is difficult for the amorphous region to bear the plastic strain, microvoids will nucleate in the amorphous regions. As a crucial mechanism for the ductile fracture of the

HEA, this unique phenomenon was also noted in a previous experimental observation [13].

When the microvoid starts to form, growth and coalescence of voids become the dominant deformation mechanism contributing to the toughening of the HEA. It can be seen from Fig. 3 that many microvoids nucleate within the amorphous regions, and the accumulated dislocations locate near the microvoids. As the deformation continues, dislocations are gradually absorbed into the surface of the microvoids and become less and less, and the connecting area between adjacent microvoids is gradually amorphized. The deformation is mainly mediated by the amorphized connecting area. The stretched amorphized connecting area becomes thinner and thinner. Finally, two voids coalesce with each other and a big void is formed. The continuous coalescence of microvoids finally leads to the overall fracture of the material. In the whole process, the strain energy is significantly dissipated, which is also an important origin of the ductile fracture of the HEA.

D. Hierarchical toughening mechanisms at CTs

In order to further clarify the mechanism of the unusually enhanced fracture toughness of the fcc-phased HEA at CTs found experimentally [13,24] and numerically in the present simulations, we also focus on the whole deformation process of the HEA at CTs. Moreover, the similarities and differences of all phenomena at RT and CTs are further compared. Figures S3 and S4 [55] show the comparative deformation and fracture process in the HEA under RT and CTs. The hierarchical toughening mechanisms found in the HEA at RT, i.e., the incipient plasticity, the local amorphous phase transformation, and the formation and dynamic evolution of microvoids, are also observed at CTs.

The apparent difference we found is the fracture behavior at level II in the HEA under different temperatures. The dislocation behaviors in HEA at RT and CTs are shown in Fig. 4. It is found that the length of total dislocation lines [Fig. 4(b)] and the length of the $\frac{1}{6}\langle 110 \rangle$ stair-rod dislocation line [Fig. 4(d)] decreases with the decrease of temperature, while the length of the $\frac{1}{6}\langle 11\bar{2} \rangle$ Shockley partial dislocation line of RT is not always lower or higher than those of CTs. The reason is that the length of mobile dislocations is dynamic. The mobile dislocations can interact with each other, and can be absorbed into the amorphous regions and the surfaces of the microvoids. The complex dislocation behaviors as well as the hierarchical toughening mechanisms contribute jointly to the dissipation of strain energy, i.e., fracture toughness, of the HEA at RT and CTs. As we know that the stair-rod dislocation is a kind of immobile dislocation, which can hinder the planar slip of Shockley partial dislocation, thus fewer stair-rod dislocations at CTs are helpful for the easier planar slip of Shockley partial dislocations. This may be a reason for the delay of the occurrence of the local amorphous phase transformation in the HEA at CTs.

E. Comparison of toughening mechanisms between the HEA and Ni at RT and CTs

To illustrate the differences between the fcc-phased HEA and traditional fcc pure metals in the temperature-dependent

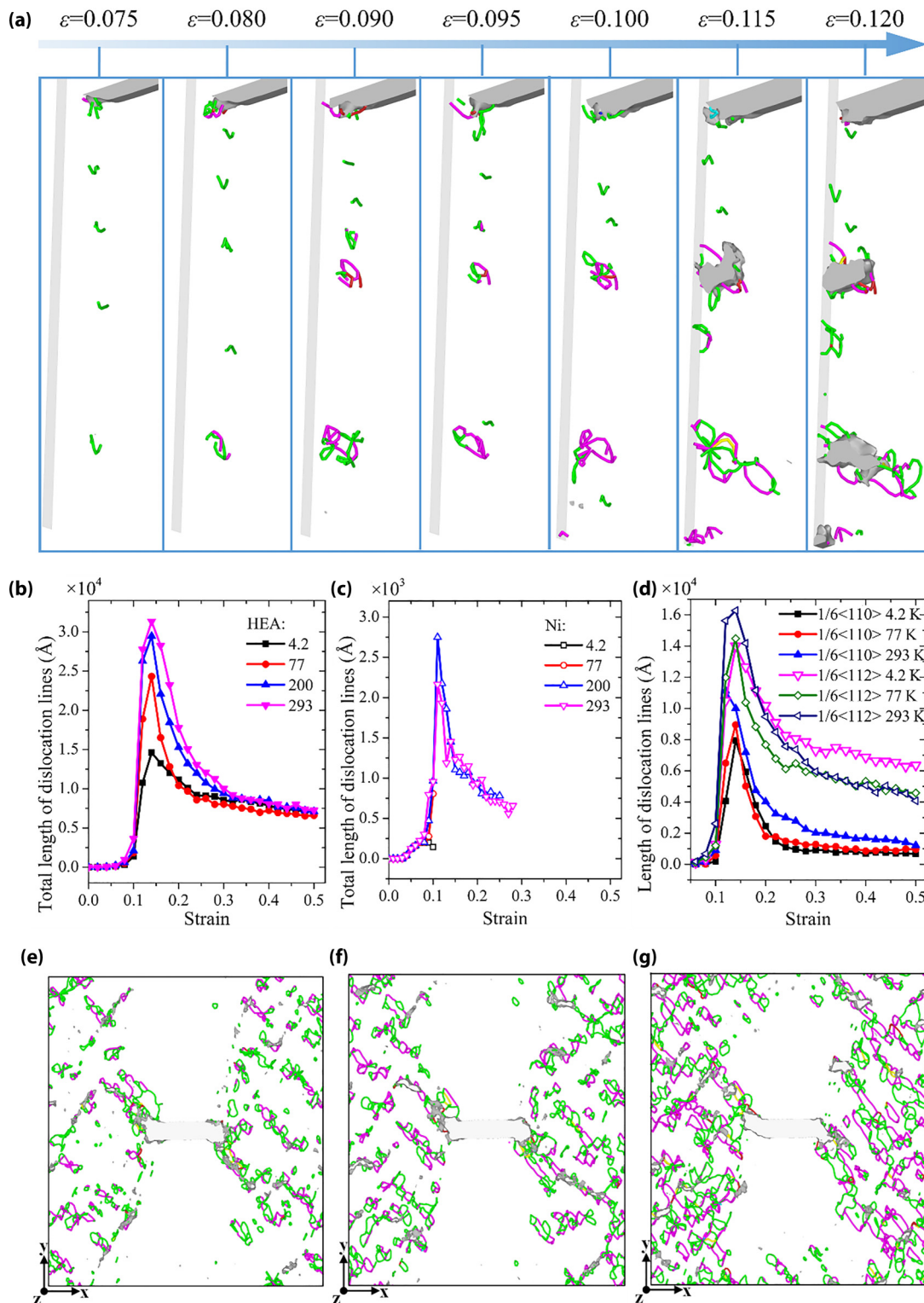


FIG. 4. Dislocation behaviors at RT and CTs. (a) Dislocation interaction near the crack tip of the HEA at RT. (b,c) Variation of total length of dislocation lines in HEA and Ni with the applied strain at RT and CTs, respectively. (d) Variation of length of Shockley partial dislocation and stair-rod dislocation in the HEA at RT and CTs, respectively. (e–g) Dislocation structures in the HEA under a strain of 12.5% at 4.2, 77, and 293 K, respectively. The dislocations in (a,e–g) are extracted and colored with the DXA method, and all the atoms are deleted for clarity.

intrinsic toughening mechanisms, we compare the deformation and fracture process in the HEA and Ni at RT and CTs.

Generally, significant difference can be found in the total dislocation numbers between the two materials at RT and

CTs, as shown in Figs. 4(b) and 4(c). When the temperature is relatively high, which here refers to more than 200 K, the trend of variation of the length in Ni is basically the same as that of the HEA, while lower temperature suppresses

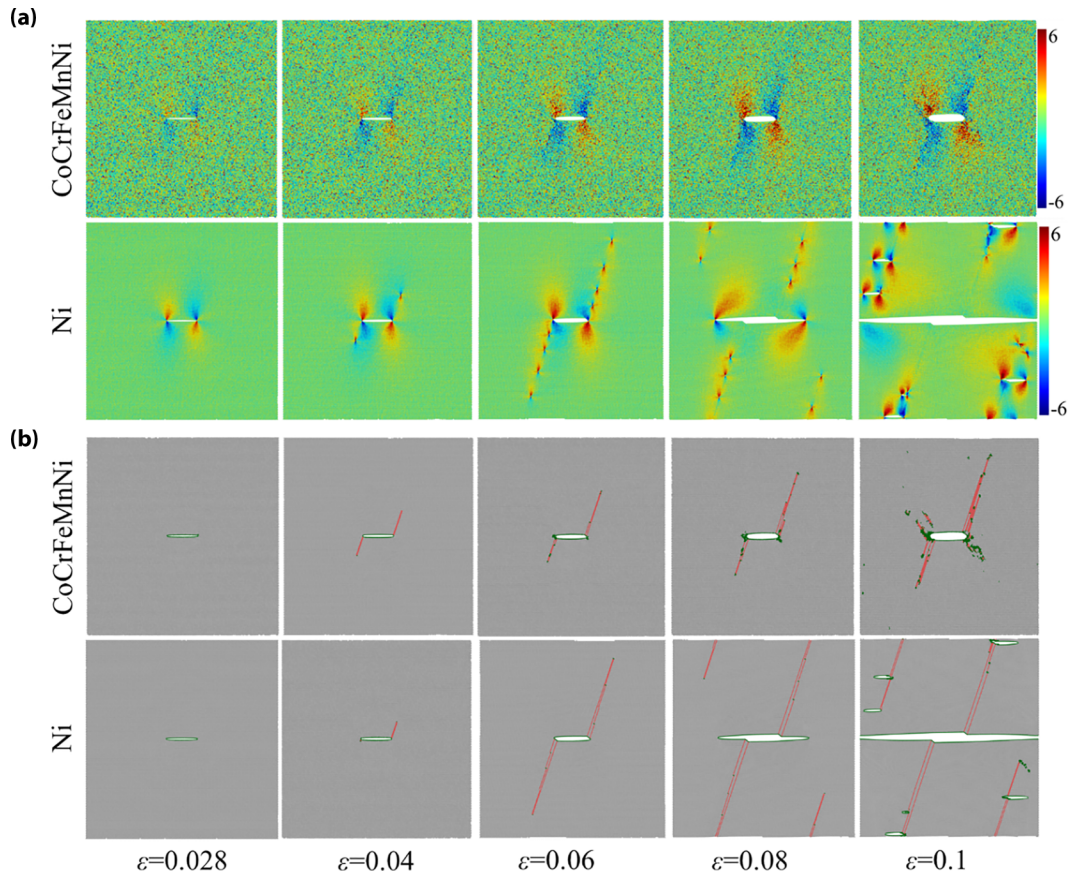


FIG. 5. Stress fields and deformation in the HEA and Ni at a CT of 4.2 K under different applied strain. (a) Atomic shear stress contours. Severe stress accumulation occurs at the crack tip and dislocation core regions in Ni, while the stress distribution is more homogeneous in the HEA. (b) Plastic deformation and crack propagation.

the formation and motion of dislocations in Ni, leading to a brittle fracture, which is totally different from the HEA. The maximum lengths of dislocation lines in HEA at RT and CTs are one and two orders of magnitude larger than those of Ni, respectively.

Figures S5 and S6 [55] compare the deformation and fracture process between the HEA and Ni at RT. The incipient plasticity in Ni is the slip of Shockley partial dislocation and the deformation twinning, while the crystalline phase transformation (level I), the local amorphization (level II), and the dynamic evolution of microvoids (level III) found in the HEA are not observed in Ni. Instead, the formation and propagation of microcracks occur in Ni (Fig. S7 [55]). The microcracks can form in the boundaries of the rotated regions and the unrotated regions, since deformation twins in Ni induce the rotation of the crystal lattice [25] (Fig. S8 [55]). The formation, propagation, and coalescence of microcracks in Ni can dissipate the strain energy stored in the material, and delay the advance of the main crack, which is also quite different from the hierarchical deformation in the HEA at RT.

When the temperature decreases from RT to CTs, the differences of deformation and fracture behaviors between the HEA and Ni become more remarkable. Figure 5 gives a comparison between the two materials at a CT of 4.2 K. At this temperature, a more severe stress concentration is observed in Ni. Consequently, it is hard for slip of dislocation to occur in Ni at CT, and the main crack propagates quickly

before the microcracks start to propagate and coalesce (Fig. S8 [55]). It should be noted that although both dislocation slip and deformation twinning are the results of dislocation activity in a material, deformation twinning contributes less to plastic strain than dislocation slip, which is not enough to blunt the sharp crack tip. Thus brittle fracture happens in Ni at CTs, which is completely different from the hierarchical deformation in the HEA at CTs.

The transition of fracture mode from ductile to brittle from RT to CT in traditional fcc Ni does not appear in the fcc-phased HEA. Competition between brittle and ductile fractures depends on the ratio between the stacking fault energy and the surface energy of a material [61]. The former is the energy needed for the nucleation and motion of dislocations, while the latter is the energy needed for the formation of new surfaces. It is known that surface energy and generalized stacking fault energy of a material are measures of the ability to form new surfaces and nucleate dislocations, respectively. Thus we calculate in Fig. 6 the surface energies and the generalized stacking fault energies of the HEA and Ni at RT and CTs. Generalized stacking fault energies of the HEA and Ni as functions of the relative displacements along the $[\bar{1}\bar{1}2]$ direction are shown in Fig. 6(c), in which the γ_{ISF} and γ_{USF} are the energy of intrinsic stacking fault and the energy of unstable stacking fault, respectively. Comparing the two curves, it can be seen that there is some difference in the values of γ_{ISF} and γ_{USF} . The γ_{ISF} of Ni and HEA are

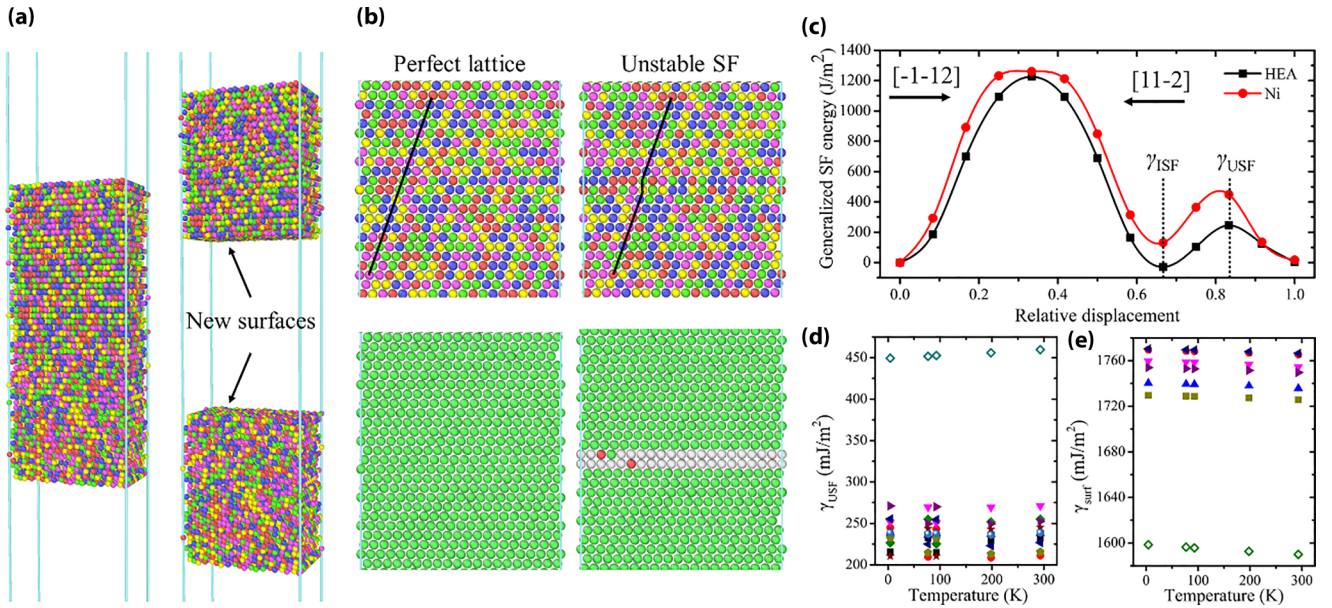


FIG. 6. Stacking fault energies and surface energies of the HEA and Ni at RT and CTs. (a) MD simulation model for calculating the surface energies of the HEA. (b) MD simulation model for calculating the generalized stacking fault energies of the HEA. The upper and lower rows are colored with element types and crystal structures, respectively. (c) Generalized stacking fault energies of the HEA and pure metal as functions of the relative displacements along the $[1\bar{1}2]$ direction. γ_{USF} and γ_{ISF} denote the energies of the unstable stacking fault and the energy of the intrinsic stacking fault, respectively. (d) The unstable stacking fault energies, γ_{USF} , of the two materials at RT and CTs. (e) The surface energies, γ_{surf} , of the two materials at RT and CTs. The solid and hollow symbols in Figs. 5(d) and 5(e) donate the energies of the HEA and traditional metal, respectively.

131.31 and -28.87 mJ/m^2 , and the γ_{USF} of Ni and HEA are 459.70 and 245.64 mJ/m^2 , respectively. The γ_{USF} is an energy barrier that needs to be overcome to form an intrinsic stacking fault. Thus it is clear that dislocations are much easier to nucleate in the HEA. In addition, the unstable stacking fault energies and surface energies of the two materials at different temperatures are shown in Figs. 6(d) and 6(e). The surface energy of Ni is significantly lower than that of the HEA, while the unstable stacking fault energy of Ni is about twice of that of the HEA, which indicates that dislocation behaviors occur much more easily in HEA instead of crack propagation, comparing with Ni.

The well-known Griffith's criterion [62] for cleavage fracture states that a crack propagates under mode I loading if the energy release rate (G_I) exceeds the energy of the newly created surfaces, $2\gamma_{\text{surf}}$. Thus the critical energy release rate is

$$G_{Ic}^G = 2\gamma_{\text{surf}}. \quad (6)$$

Taking into account crack tip plasticity, Rice's criterion [61] considers the contribution of the unstable stacking fault energy (γ_{USF}) as the barrier for dislocation emission and motion. For mode I loading, the criterion is written as

$$G_{Ic}^R = 8 \frac{1 + (1 - \nu)\tan^2\varphi}{(1 + \cos\theta)\sin^2\theta} \gamma_{\text{USF}}, \quad (7)$$

where θ and φ are the angles between the crack direction and the slip plane, and the slip direction and the normal to crack front, and ν is Poisson's ratio. Hence, ductile fracture should

occur if $G_{Ic}^G > G_{Ic}^R$; i.e.,

$$\frac{\gamma_{\text{surf}}}{\gamma_{\text{USF}}} > 4 \frac{1 + (1 - \nu)\tan^2\varphi}{(1 + \cos\theta)\sin^2\theta}. \quad (8)$$

In the present work, $\theta = 70.5^\circ$ and $\varphi = 0^\circ$; taking $\nu = 0.3$, we have $\frac{\gamma_{\text{surf}}}{\gamma_{\text{USF}}} > 3.375$. Thus ductile fracture should happen if the ratio is much higher than 3.375, brittle fracture should happen if the ratio is much lower than 3.375, and both fracture modes may occur simultaneously if the ratio is comparable to 3.375. According to the results in Figs. 5(d) and 5(e), the ratios of Ni at RT and 4.2 K are 3.459 and 3.557, respectively, and those of the HEA are 7.33 and 7.355, respectively, indicating ductile fracture is the main mode in the HEA at both RT and CTs, while both fracture modes can occur in Ni. The fracture modes predicted with the theoretical criteria are consistent with our atomistic simulations.

IV. DISCUSSION

Our work provides evidence for the excellent intrinsic fracture toughness of the fcc-phased HEA at both RT and CTs. The hierarchical toughening mechanisms can be summarized in Fig. S9 in the Supplemental Material [55]. As the strain is increased, the multiple mechanisms can continually take place near the crack tip when subjected to external loading. Triggering the next mechanism requires the generation and evolution of additional crystal defects, leading to increased deformation energy, i.e., fracture toughness.

In fact, the hierarchical toughening mechanisms are based on the nucleation, motion, and interaction of dislocations. These complex dislocation behaviors are affected by the

stacking fault energy, as well as the lattice distortion. Lower unstable stacking fault energy can promote dislocation activities, and more severe lattice distortion can promote dislocation interactions. On the other hand, lattice distortion may affect the fluctuation of local stacking fault energy, which in turn affects the motion of dislocations. In the previous experiment [58], the Mn element in fcc-phased CoCrFeMnNi HEA is replaced by the Pd element, in which the atomic size of Pd is apparently larger than that of Mn. This treatment can increase the inhomogeneity of atomic size, which brings about larger lattice distortion. *In situ* TEM during the straining experiment [58] reveals massive dislocation cross slips from the early stage of plastic deformation, resulting in strong dislocation interactions between multiple slip systems. More recently, the synergy of strength and ductility of fcc-phased CoNi alloy is achieved by compositional undulation, which renders the stacking fault energy and lattice distortion, such that the motion of dislocations is thus significantly affected [63]. The experimental results also confirm our conclusion. Thus triggering the hierarchical mechanisms requires not only low unstable stacking fault energy but also severe lattice distortion. By tailoring the composition and distribution of atoms, which may reduce the unstable stacking fault energy and increase the lattice distortion, the intrinsic fracture toughness of multicomponent alloys (not limited to fcc-phased HEAs) can be enhanced, especially in cryogenic service environments.

V. CONCLUSION

In conclusion, the intrinsic toughening mechanism for the fcc-phased HEAs is systematically investigated using CoCrFeMnNi as a model system. The hierarchical toughening mechanisms, including the slip of partial dislocations; the deformation twinning; the crystalline phase transformation; the dislocation interaction; the local amorphous phase transformation; and the formation, growth, and coalescence of microvoids, are revealed at both RT and CTs, which results in the continuous dissipation of strain energy. In addition, fewer immobile dislocations in the HEA at CTs may be a reason for the delay of the occurrence of the local amorphous phase transformation and microvoids, leading to higher fracture toughness. The differences in mechanisms for the low-temperature toughening of the HEA and low-temperature embrittlement of traditional metals are further comparatively revealed. Our study provides mechanistic insights into the fundamental understanding of toughening mechanisms in the fcc-phased CoCrFeMnNi HEA at RT and CTs, which provide guidance for design of high-performance alloys to withstand extreme service environments.

ACKNOWLEDGMENT

This work is supported by NSFC (Grants No. 12002035, No. 12032004, No. 12102121, No. 12272043, and No. 11932004).

-
- [1] W. Li, D. Xie, D. Li, Y. Zhang, Y. Gao, and P. K. Liaw, *Prog. Mater. Sci.* **118**, 100777 (2021).
 - [2] Y. Zhang, T. T. Zuo, Z. Tang, M. C. Gao, K. A. Dahmen, P. K. Liaw, and Z. P. Lu, *Prog. Mater. Sci.* **61**, 1 (2014).
 - [3] J.-W. Yeh, S.-K. Chen, S.-J. Lin, J.-Y. Gan, T.-S. Chin, T.-T. Shun, C.-H. Tsau, and S.-Y. Chang, *Adv. Eng. Mater.* **6**, 299 (2004).
 - [4] B. Cantor, I. T. H. Chang, P. Knight, and A. J. B. Vincent, *Mater. Sci. Eng.: A* **375–377**, 213 (2004).
 - [5] C. Huang, Y. Yao, and S. Chen, *ACS Omega* **7**, 29675 (2022).
 - [6] M.-H. Tsai and J.-W. Yeh, *Mater. Res. Lett.* **2**, 107 (2014).
 - [7] Q. Zhang, R. Huang, X. Zhang, T. Cao, Y. Xue, and X. Li, *Nano Lett.* **21**, 3671 (2021).
 - [8] S. Wei, S. J. Kim, J. Kang, Y. Zhang, Y. Zhang, T. Furuhashi, E. S. Park, and C. C. Tasan, *Nat. Mater.* **19**, 1175 (2020).
 - [9] Q. Zhang, R. Huang, J. Jiang, T. Cao, Y. Zeng, J. Li, Y. Xue, and X. Li, *J. Mech. Phys. Solids* **162**, 104853 (2022).
 - [10] D. Wei, X. Li, S. Schönecker, J. Jiang, W.-M. Choi, B.-J. Lee, H. S. Kim, A. Chiba, and H. Kato, *Acta Mater.* **181**, 318 (2019).
 - [11] P. Shi, W. Ren, T. Zheng, Z. Ren, X. Hou, J. Peng, P. Hu, Y. Gao, Y. Zhong, and P. K. Liaw, *Nat. Commun.* **10**, 489 (2019).
 - [12] Z. Zhang, H. Sheng, Z. Wang, B. Gludovatz, Z. Zhang, E. P. George, Q. Yu, S. X. Mao, and R. O. Ritchie, *Nat. Commun.* **8**, 14390 (2017).
 - [13] B. Gludovatz, A. Hohenwarter, D. Catoor, E. H. Chang, E. P. George, and R. O. Ritchie, *Science* **345**, 1153 (2014).
 - [14] P. Shi, R. Li, Y. Li, Y. Wen, Y. Zhong, W. Ren, Z. Shen, T. Zheng, J. Peng, X. Liang *et al.*, *Science* **373**, 912 (2021).
 - [15] E. P. George, W. A. Curtin, and C. C. Tasan, *Acta Mater.* **188**, 435 (2020).
 - [16] E. Lu, I. Makkonen, K. Mizohata, Z. Li, J. Räsänen, and F. Tuomisto, *J. Appl. Phys.* **127**, 025103 (2020).
 - [17] L. Jiang, Y. Hu, K. Sun, P. Xiu, M. Song, Y. Zhang, W. L. Boldman, M. L. Crespillo, P. D. Rack, L. Qi *et al.*, *Adv. Mater.* **32**, e2002652 (2020).
 - [18] F. Maresca and W. A. Curtin, *Acta Mater.* **182**, 235 (2020).
 - [19] J. Li, S. Chen, G. J. Weng, and W. Lu, *Int. J. Plast.* **144**, 103024 (2021).
 - [20] Q. Huang, Q. Zhu, Y. Chen, M. Gong, J. Li, Z. Zhang, W. Yang, J. Wang, H. Zhou, and J. Wang, *Nat. Commun.* **12**, 6695 (2021).
 - [21] J. Li, G. J. Weng, S. Chen, and X. Wu, *Int. J. Plast.* **88**, 89 (2017).
 - [22] J. Li, W. Lu, J. Gibson, S. Zhang, S. Korte-Kerzel, and D. Raabe, *Scr. Mater.* **179**, 30 (2020).
 - [23] F. Otto, A. Dlouhý, C. Somsen, H. Bei, G. Eggeler, and E. P. George, *Acta Mater.* **61**, 5743 (2013).
 - [24] B. Gludovatz, A. Hohenwarter, K. V. Thurston, H. Bei, Z. Wu, E. P. George, and R. O. Ritchie, *Nat. Commun.* **7**, 10602 (2016).
 - [25] M. A. Meyers and K. K. Chawla, *Mechanical Behavior of Materials* (Cambridge University Press, Cambridge, New York, 2009).
 - [26] L. Pei, C. Lu, K. Tieu, X. Zhao, L. Zhang, K. Cheng, and G. Michal, *Mater. Lett.* **152**, 65 (2015).
 - [27] P. Gumbsch, J. Riedle, A. Hartmaier, and H. F. Fischmeister, *Science* **282**, 1293 (1998).

- [28] Z. Zhang, M. M. Mao, J. Wang, B. Gludovatz, Z. Zhang, S. X. Mao, E. P. George, Q. Yu, and R. O. Ritchie, *Nat. Commun.* **6**, 10143 (2015).
- [29] Y. Zeng, Q. Zhang, Y. Wang, J. Jiang, H. Xing, and X. Li, *Phys. Rev. Lett.* **127**, 066101 (2021).
- [30] S. Plimpton, *J. Comput. Phys.* **117**, 1 (1995).
- [31] W.-M. Choi, Y. H. Jo, S. S. Sohn, S. Lee, and B.-J. Lee, *npj Comput. Mater.* **4**, 1 (2018).
- [32] S. Shuang, S. Lu, B. Zhang, C. Bao, Q. Kan, G. Kang, and X. Zhang, *Comput. Mater. Sci.* **195**, 110495 (2021).
- [33] Q. Fang, Y. Chen, J. Li, C. Jiang, B. Liu, Y. Liu, and P. K. Liaw, *Int. J. Plast.* **114**, 161 (2019).
- [34] C. Huang, Y. Yao, X. Peng, and S. Chen, *Nanotechnology* **32**, 505724 (2021).
- [35] P. Murali, T. F. Guo, Y. W. Zhang, R. Narasimhan, Y. Li, and H. J. Gao, *Phys. Rev. Lett.* **107**, 215501 (2011).
- [36] P. Zhang *et al.*, *Nat. Commun.* **5**, 3782 (2014).
- [37] Y. Zhou, W. Yang, M. Hu, and Z. Yang, *Comput. Mater. Sci.* **112**, 27 (2016).
- [38] Z. Yang, Y. Zhou, T. Wang, Q. Liu, and Z. Lu, *Comput. Mater. Sci.* **82**, 17 (2014).
- [39] H. Y. Song and Y. L. Li, *Comput. Mater. Sci.* **111**, 125 (2016).
- [40] A. Stukowski, *Modell. Simul. Mater. Sci. Eng.* **18**, 015012 (2010).
- [41] A. Stukowski, V. V. Bulatov, and A. Arsenlis, *Modell. Simul. Mater. Sci. Eng.* **20**, 085007 (2012).
- [42] P. M. Larsen, S. Schmidt, and J. Schiøtz, *Modell. Simul. Mater. Sci. Eng.* **24**, 055007 (2016).
- [43] C. Huang, X. Peng, B. Yang, S. Weng, Y. Zhao, and T. Fu, *Comput. Mater. Sci.* **157**, 67 (2019).
- [44] Y. Zhao, X. Peng, T. Fu, C. Huang, H. Xiang, N. Hu, and C. Yan, *Materialia* **2**, 148 (2018).
- [45] C. L. Kelchner, S. J. Plimpton, and J. C. Hamilton, *Phys. Rev. B* **58**, 11085 (1998).
- [46] J. Li, Y. Chen, Q. He, X. Xu, H. Wang, C. Jiang, B. Liu, Q. Fang, Y. Liu, Y. Yang *et al.*, *Proc. Natl. Acad. Sci. USA* **119**, e2200607119 (2022).
- [47] S. Liu and Y. Wei, *Extreme Mech. Lett.* **11**, 84 (2017).
- [48] Y. Liu and X. Chen, *J. Appl. Phys.* **115**, 034303 (2014).
- [49] D. Cohen-Tanugi and J. C. Grossman, *Nano Lett.* **14**, 6171 (2014).
- [50] T. Zhang, X. Li, S. Kadkhodaei, and H. Gao, *Nano Lett.* **12**, 4605 (2012).
- [51] Z. You, X. Li, L. Gui, Q. Lu, T. Zhu, H. Gao, and L. Lu, *Acta Mater.* **61**, 217 (2013).
- [52] H. Zhou, P. Zhu, W. Yang, and H. Gao, *J. Mech. Phys. Solids* **159**, 104746 (2022).
- [53] Z. Zhang, Q. Fu, J. Wang, R. Yang, P. Xiao, F. Ke, and C. Lu, *Mater. Today Commun.* **27**, 107451 (2021).
- [54] Z. Zhang, Q. Fu, J. Wang, R. Yang, P. Xiao, F. Ke, and C. Lu, *Int. J. Solids Struct.* **228**, 111128 (2021).
- [55] See Supplemental Material at <http://link.aps.org/supplemental/10.1103/PhysRevB.107.174103> for the supplemental figures and the corresponding brief descriptions.
- [56] Y. A. Shin, S. Yin, X. Li, S. Lee, S. Moon, J. Jeong, M. Kwon, S. J. Yoo, Y. M. Kim, T. Zhang *et al.*, *Nat. Commun.* **7**, 10772 (2016).
- [57] M. Yang, L. Zhou, C. Wang, P. Jiang, F. Yuan, E. Ma, and X. Wu, *Scr. Mater.* **172**, 66 (2019).
- [58] Q. Ding, Y. Zhang, X. Chen, X. Fu, D. Chen, S. Chen, L. Gu, F. Wei, H. Bei, Y. Gao *et al.*, *Nature (London)* **574**, 223 (2019).
- [59] Q. J. Li, H. Sheng, and E. Ma, *Nat. Commun.* **10**, 3563 (2019).
- [60] S. Zhao, Z. Li, C. Zhu, W. Yang, Z. Zhang, D. E. J. Armstrong, P. S. Grant, R. O. Ritchie, and M. A. Meyers, *Sci. Adv.* **7**, eabb3108 (2021).
- [61] J. R. Rice, *J. Mech. Phys. Solids* **40**, 239 (1992).
- [62] A. A. Griffith, *Philos. Trans. R. Soc. London, Ser. A* **221**, 163 (1921).
- [63] H. Li, H. Zong, S. Li, S. Jin, Y. Chen, M. J. Cabral, B. Chen, Q. Huang, Y. Chen, Y. Ren *et al.*, *Nature (London)* **604**, 273 (2022).